A&A 379, 740–754 (2001)
DOI: 10.1051/0004-6361:20011341

Astronomy & Astrophysics

ESO imaging survey

Deep public survey: Multi-color optical data for the Chandra Deep Field South⋆

S. Arnouts[1], B. Vandame[1], C. Benoist[2], M. A. T. Groenewegen[1], L. da Costa[1], M. Schirmer[3], R. P. Mignani[1], R. Slijkhuis[1], E. Hatziminaoglou[1], R. Hook[1], R. Madejsky[1,4], C. Rité[5], and A. Wicenec[1]

[1] European Southern Observatory, Karl-Schwarzschild-Str. 2, 85748 Garching b. München, Germany
[2] Observatoire de la Côte d'Azur, BP 229, 06304 Nice Cedex 4, France
[3] Max-Planck-Institut für Astrophysik, Karl-Schwarzschild-Str. 1, 85748 Garching b. München, Germany
[4] Universidade Estadual de Feira de Santana, Campus Universitário, Feira de Santana, BA, Brazil
[5] Observatório Nacional, Rua Gen. José Cristino 77, Rio de Janerio, Brasil

Received 5 March 2001 / Accepted 17 September 2001

Abstract. This paper presents multi-passband optical data obtained from observations of the Chandra Deep Field South (CDF-S), located at $\alpha \sim 3^{\rm h}32^{\rm m}$, $\delta \sim -27°48'$. The observations were conducted at the ESO/MPG 2.2 m telescope at La Silla using the 8k × 8k Wide-Field Imager (WFI). This data set, taken over a period of one year, represents the first field to be completed by the ongoing Deep Public Survey (DPS) being carried out as a part of the ESO Imaging Survey (EIS) project. This paper describes the optical observations, the techniques employed for un-supervised pipeline processing and the general characteristics of the final data set. Image processing has been performed using multi-resolution image decomposition techniques adapted to the EIS pipeline. The automatic processing steps include standard de-bias and flat-field, automatic removal of satellite tracks, de-fringing/sky-subtraction, image stacking/mosaicking and astrometry. Stacking of dithered images is carried out using pixel-based astrometry which enables the efficient removal of cosmic rays and image defects, yielding remarkably clean final images. The final astrometric calibration is based on a pre-release of the GSC-II catalog and has an estimated intrinsic accuracy of $\lesssim$0.10 arcsec, with all passbands sharing the same solution. The paper includes data taken in six different filters ($U'UBVRI$). The data cover an area of about 0.25 square degrees reaching 5σ limiting magnitudes of $U'_{AB} = 26.0$, $U_{AB} = 25.7$, $B_{AB} = 26.4$, $V_{AB} = 25.4$, $R_{AB} = 25.5$ and $I_{AB} = 24.7$ mag, as measured within a $2 \times FWHM$ aperture. The optical data covers an area of ∼0.1 square degrees for which moderately deep observations in two near-infrared bands are also available, reaching 5σ limiting magnitudes of $J_{AB} \sim 23.4$ and $K_{AB} \sim 22.6$. The current optical/infrared data also fully encompass the region of the deep X-ray observations recently completed by the Chandra telescope. The optical data presented here, as well as the infrared data released earlier, are publicly available world-wide in the form of fully calibrated pixel and associated weight maps and source lists extracted in each passband. These data can be requested through the URL "`http://www.eso.org/eis`".

Key words. catalogs – surveys – stars: general – galaxies: general

1. Introduction

The successful application of photometric techniques to identify high-redshift galaxies ($z \gtrsim 3$), combined with large-aperture telescopes with multi-object spectrographs, have provided the means to study large-scale structures at high-redshifts and to directly probe their evolution over a broad range of redshifts. Currently, the challenge is to construct well-defined statistical galaxy samples at faint magnitudes and use photometric redshift techniques to pre-select candidates for large spectroscopic surveys probing the high-redshift Universe. To achieve this goal, deep optical/infrared multi-passband surveys covering areas of the order of a few degrees are required.

Interest in this type of dataset is widespread in Europe given the imminent commissioning of the multi-object spectrograph VIMOS, part of the new generation of VLT instruments. Foreseeing this need, the Working

Send offprint requests to: S. Arnouts,
e-mail: `sarnouts@eso.org`

⋆ Based on observations collected at the European Southern Observatory, La Silla, Chile within program ESO 164.O-O561.

Group (WG) for public surveys at ESO recommended in early 1999 the undertaking of a deep, multi-passband, optical survey covering three separate regions of sky one square degree each, with some areas also covered in the infrared. These regions, referred to as Deep-1, 2 and 3, are located over a wide range of right ascension and each corresponds to four adjacent pointings (a–d) of the Wide-Field Imager (WFI) mounted on the 2.2 m MPG/ESO telescope at La Silla. The main goal of the survey is to produce suitable statistical samples to study large-scale structures in the redshift domains $z \lesssim 1$ and $z \gtrsim 3$. Details of the position of the selected regions can be found at the URL "`http://www.eso.org/science/eis/`". One of the selected regions includes the Chandra Deep Field South (CDF-S; Giacconi et al. 2001) chosen because of its low column-density of hydrogen and absence of bright stars, characteristics that make it well-suited for deep X-ray observations with the Chandra (AXAF) telescope. These observations have recently been completed for a total integration time of one million seconds producing the deepest high-resolution X-ray image ever taken (Rosati et al. 2001).

In this paper, the *UBVRI* optical observations with the WFI of one of the selected fields (Deep-2c), covering the CDF-S, are presented. These data are used to make a first assessment of the procedures and overall performance of the optical part of the Deep Public Survey (DPS). The optical data presented here complement those in the near-infrared covering an area of ∼0.11 square degrees (Vandame et al. 2001) encompassing the region covered by the Chandra observations. The new data reported here extend earlier optical/infrared observations of this field carried out by EIS at the NTT in 1998, covering a considerably smaller region. These older data are currently being re-analyzed to produce, together with the new data, a homogeneous dataset (Benoist et al. 2001a) which will supersede the earlier 1998 release (Rengelink et al. 1998). Section 2 reviews the overall observing strategy and describes the observations. Section 3 discusses the techniques employed in the data reduction and the photometric and astrometric calibration of the images. While other derived products are expected to be made available in the near future, only photometric parameters of the sources detected in each of the available passbands are presented for the moment in Sect. 4. Even though the goal of the present paper is not to interpret the data being released, Sect. 5 presents the results of comparisons between the present observations and those of other authors. This is done for the sole purpose of assessing the quality of the astrometry and photometry of the present data set and its adequacy to meet the main goals of the survey. Finally, a brief summary is presented in Sect. 6.

2. Observations

The optical observations of the CDF-S region ($\alpha \sim 3^{\rm h}32^{\rm m}$, $\delta \sim -27^{\rm o}48'$) were carried out using the WFI camera at the Cassegrain focus of the MPG/ES0 2.2 m telescope at the La Silla observatory. WFI is a focal reducer-type mosaic camera with 4×2 CCD chips. Each chip is composed of a 2048×4098 pixel array and covers a field of view of 8.12×16.25 arcmin with a projected pixel size of 0.238 arcsec. The 8 CCDs are physically separated by gaps of width 23.8 and 14.3 arcsec along the right ascension and declination directions, respectively. The full field of view of the camera is thus 34×33 arcmin, with a filling factor of 95.9%. Details on the WFI layout can be found, for instance, at the URL "`http://www.eso.org/science/eis/eis_proj/public/wfi_chip.html`" as well as at other locations on the ESO web pages.

Observations of the CDF-S have been performed using the WFI filters summarized in Table 1. The *U*-band observations were originally conducted using the available narrow filter which was recently (October 2000) replaced by a broader filter to increase the efficiency of the survey. The transmission curves of these filters are plotted in Fig. 1 together with their final throughputs taking into account the optics and the CCD quantum efficiency. It is worth mentioning that very little was known about the performance of the instrument at the time the survey was conceived, especially at the blue and red ends of the wavelength range considered.

Table 1. Filters used in the observations of the CDF-S.

Filter	ESO id	$\lambda_{\rm eff}$ (Å)	*FWHM* (Å)
U	*U*/38	3710	325
U′	*U*350/60	3538	560
B	*B*/99	4556	905
V	*V*/89	5342	900
R	*R*c/162	6402	1595
I	*I*c/lwp	8535	1387

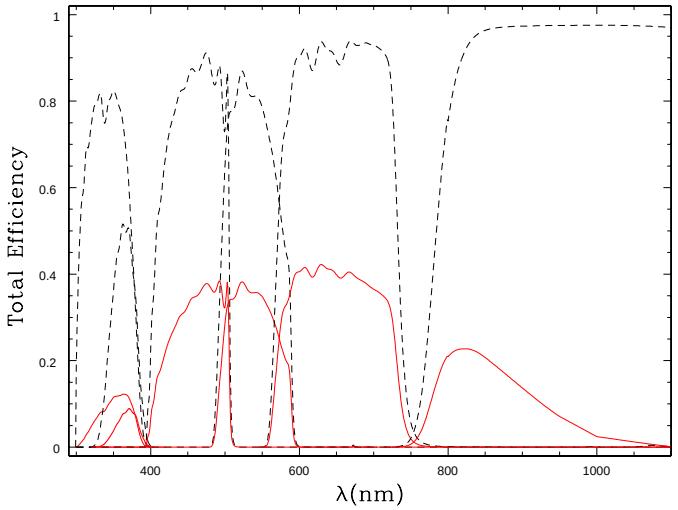

Fig. 1. Transmission curves of the filters (dashed line) and the total throughput of the system (solid line).

The observations in each passband were split into observation blocks (OBs) consisting of a sequence of five exposures with the integration time for each individual exposure ranging from 5 to 15 min depending on the passband. Table 2 summarizes the planned observational strategy, listing: in Col. 1 the passband; in Col. 2 the integration time of each individual exposure; in Col. 3 the number of exposures per OB; in Col. 4 the integration time per OB; in Col. 5 the number of OBs; and in Col. 6 the planned total integration time per band. According to the planned strategy, a total of 210 WFI frames were required to complete a single pointing. In order to minimize the imprint of the inter-chip gaps the choice of pointings were done in the following way. First, the nominal position of each OB (in a given passband) was drawn from a pre-defined list of distinct positions, as given in Table 3. For instance, in the case of U-band which requires 13 OBs, the dithering pattern used is illustrated in Fig. 2. Next, each exposure in the OB sequence was dithered relative to the OB reference position using the offsets in right ascension ($\Delta\alpha\cos\delta$) and in declination ($\Delta\delta$) as listed in Table 4 and illustrated in the inset of Fig. 2. This dithering is essential for de-fringing as well as for efficiently removing cosmic rays and other CCD blemishes.

Table 2. Planned Observing Strategy for the CDF-S observations.

Filter	$T_{\rm tot}$ (s)	$N_{\rm OB}$	$T_{\rm exp}$ (s)
U	60 000	13	900
B	12 000	8	300
V	9000	6	300
R	9000	6	300
I	27 000	9	600

The optical observations span six observing runs over a period of one year (ESO observing periods 64 and 66), distributed over a total of 12 nights. The log of the observations is summarized in Table 5. The table lists: in Col. 1 the date of the observations; in Col. 2 the passband; in Col. 3 the integration time; and in Cols. 4 and 5 the range and average seeing during the night as measured by the seeing monitor. Not listed are the B-band observations taken during the commissioning phase of the WFI, in January 1999, and the U-band data of the COMBO survey (Wolf et al. 2001). Both data sets have been re-processed, for the sake of homogeneity, and used to produce the final combined images. Table 6 summarizes the data available for the CDF-S used in this paper. The table lists: in Col. 1 the band; in Col. 2 the total integration time; in Col. 3 the total number of frames; and in Col. 4 the average seeing of the final co-added images.

To assess the effectiveness of the adopted dithering pattern, Fig. 3 illustrates the exposure time map associated with the final R-band image which is an example of one of the passbands with the shortest exposure and is

Table 3. Nominal coordinates of OBs (see text for definition).

ID	α(J2000)	δ(J2000)
01	03:32:28	−27:48:47
02	03:32:34	−27:48:17
03	03:32:36	−27:49:02
04	03:32:32	−27:49:32
05	03:32:23	−27:49:17
06	03:32:21	−27:48:31
07	03:32:25	−27:48:02
08	03:32:30	−27:47:47
09	03:32:27	−27:49:47
10	03:32:19	−27:50:02
11	03:32:38	−27:47:32
12	03:32:40	−27:50:17
13	03:32:17	−27:47:17

Table 4. Relative offsets of each exposure in a OB.

Dith. #	$\Delta\alpha\cos\delta(''$)	$\Delta\delta(''$)
1	0	0
2	−70	+21
3	−35	−42
4	+35	+42
5	+70	−21

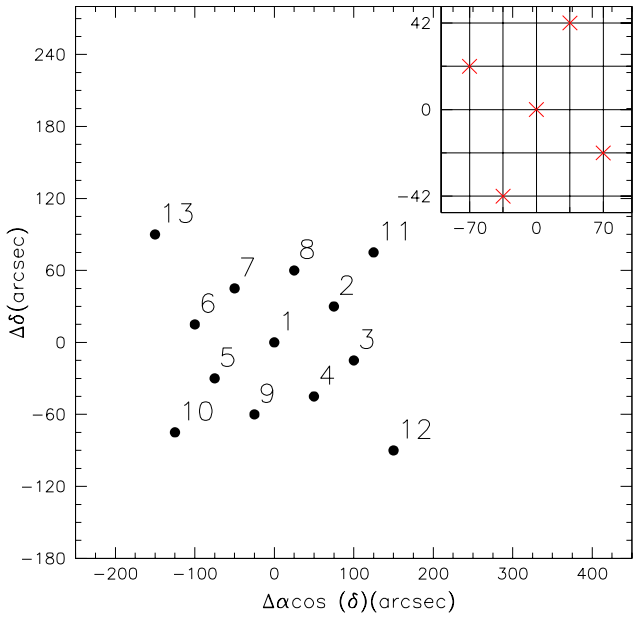

Fig. 2. Schematic view of the dithering pattern used in the observations. Large filled circles mark the coordinates of each OB relative to the nominal center of the field (OB #1 in Table 3). *Inset*: the crosses mark the offset, in arcsec, of each single exposure within an OB, with respect to its center.

Table 5. Log of observations.

Date	Filter	T (s)	seeing range (arcsec)	mean seeing (arcsec)
Nov. 04 1999	U	11 700	0.62–0.97	0.77
	I	8400	0.77–1.71	1.04
Nov. 05 1999	U	13 500	0.74–0.94	0.82
Nov. 06 1999	U	14 400	0.48–0.83	0.64
Nov. 07 1999	I	17 700	0.76–1.26	0.97
Nov. 08 1999	V	13 500	1.40–1.81	1.61
	I	6000	1.20–2.08	1.64
Dec. 03 1999	V	6000	0.46–0.98	0.66
Dec. 04 1999	V	3000	0.48–0.72	0.58
	R	9000	0.47–0.79	0.58
	I	1800	0.67–0.77	0.71
Oct. 26 2000	U'	13 000	0.57–1.04	0.78
Oct. 27 2000	U'	11 700	0.52–1.01	0.70
Nov. 27 2000	U'	9000	0.50–0.76	0.59
Nov. 28 2000	U'	9000	0.67–1.06	0.87
Nov. 29 2000	U'	4500	0.66–1.88	0.76

Table 6. Summary of the CDF-S observations.

Filter	$T_{\rm eff}$ (s)	$N_{\rm f}$	Seeing (arcsec)
U	47 600	55	0.98
U'	43 600	49	1.06
$B^{\rm a}$	24 500	30	1.02
V	9250	33	0.97
R	9250	33	0.86
I	26 900	46	0.93

[a] Commissioning data

thus the least homogeneous (see Sect. 5). In this particular case, the flux ratio of the best sampled region to that at the center of the image is a factor ∼2. This is due in part to the clipping (∼200 pixels) of the CCD frames not taken into account in the original design of the dithering pattern. In the weight-map the effects of at least three satellite tracks can be seen. It is important to point out that some of the survey data have been obtained using dithering patterns different from the one shown in Fig. 3 (e.g., the B-images taken during the commissioning of WFI). In fact, during the course of the survey the pattern has been changed at least once to improve the uniformity of the final image.

The present optical survey complements both recent infrared observations reported by Vandame et al. (2001) as well as optical/infrared observations conducted as part of the EIS-DEEP survey first released in 1998 (Rengelink et al. 1998) and currently under revision

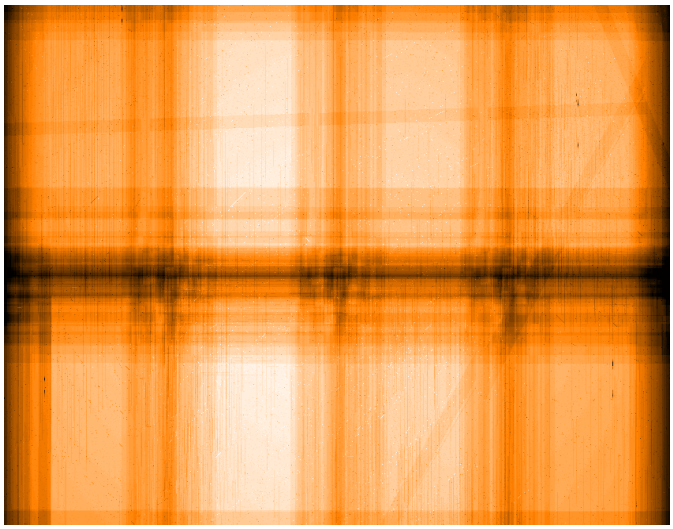

Fig. 3. Weight map corresponding to the final co-added R-band image. The bright regions correspond to locations in the image which have higher sensitivity. While the effect of the inter-chip gaps are minimized, their imprint can still be seen and correspond to the darkest regions of the map (see text for more details). Also note the slightly lower sensitivity in regions where satellite tracks have been detected in individual frames and removed. At least two of them are clearly seen on the upper part and on the right side of the weight map, respectively.

(Benoist et al. 2001a). The coverage of this field by these different sets of data is shown schematically in Fig. 4.

3. Data reduction

3.1. Pipeline processing

The WFI images were processed using the refurbished EIS pipeline (e.g., da Costa et al. 1999; da Costa 2001) which includes new operational modules to enable unsupervised pipeline reduction of WFI images as well as new software routines for carrying out the basic steps of image processing and calibration. Given the scope of the surveys being carried out by EIS, special attention has been given to the development of a survey software system to ensure the adequate and timely processing of large amounts of data for long periods of time in a uniform way. For instance, the complete DPS survey will consist of some 2800 WFI science frames representing over 1 Terabyte of data, to which should be added a comparable amount of data from the so-called Pre-Flames survey not discussed here (Momany et al. 2001). While a detailed account of the extent of these changes is beyond the scope of the present paper, some of the main features are briefly summarized below.

One of the main changes has been the complete removal of different IRAF packages (e.g., xccdred, drizzle) used earlier to process images from CCD mosaics and in the co-addition phase. Instead, WFI images are now split into individual chips at the very beginning of the process. The main advantages of adopting this procedure are that

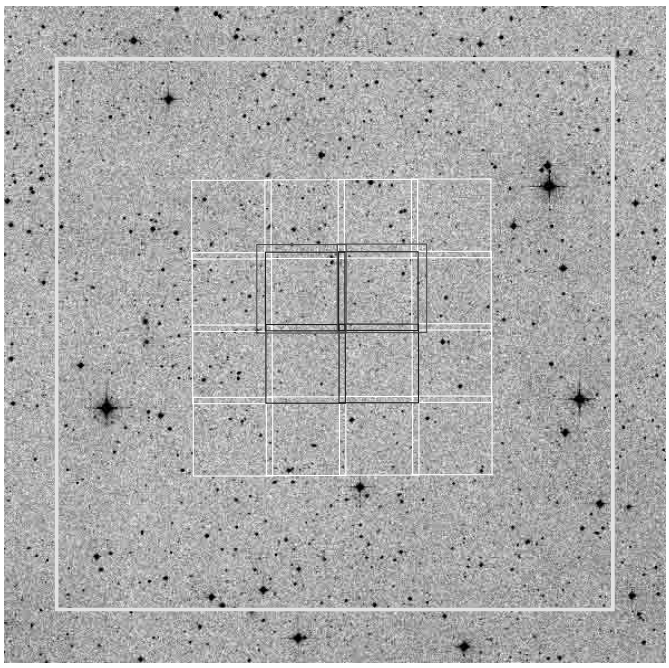

Fig. 4. Schematic view of the coverage of the CDF-S by the EIS program using different instruments. The outer white box delineates the coverage of the present optical survey (WFI). The 2×2 black mosaic and the two overlapping gray boxes delineate the area covered by the infrared (SOFI) and optical (SUSI2) observations, respectively, carried out by EIS-DEEP survey at the NTT. Finally, the 4×4 white mosaic represents the complete infrared coverage, including the Deep Public Survey data presented by Vandame et al. (2001). The background image is taken from the DSS.

the pipeline uses a common library of routines, single and multi-chip images are treated in the same way and that the EIS pipeline is more easily adaptable to use PC-based Linux clusters for parallel-processing images, which will eventually lead to a higher throughput.

A major effort has also been made to address specific problems encountered with the data files coming from WFI. These have constantly evolved, which makes them difficult to handle from the point of view of a pipeline. One of the main challenges has been the lack of information in the FITS header regarding the reference pixel. This prevented the unsupervised reduction of the WFI data due to frequent failures in the astrometric calibration from run to run. As the EIS observations with WFI span a long period of time (over two years), during which several upgrades of the data acquisition were made, it was necessary to develop robust procedures to cope with these various changes automatically.

Using tools available from the multi-resolution visual model package (MVM) developed by Bijaoui and collaborators, a special routine was developed to find a first-order astrometric solution for an image, searching a large (∼6×) area surrounding the nominal position of the pointing. The method uses one of the science frames in the run and takes the available information in the image header regarding the pointing only as a first guess. This image is quickly reduced and decomposed using a wavelet transform. The lowest resolution component is then used to cross-correlate features against a low-resolution mock image representing the reference catalog over a much larger area than the original image. The low-resolution science image is then moved around in a spiral pattern starting from its nominal position as given in the image header. At each step a cross-correlation function between the features in the real and mock images is computed and the process resumed. At the end of the search, the position with the largest amplitude of the cross-correlation is used to define a first approximation for the location of the reference pixel for that run. This procedure is aimed at correcting only for large shifts. A more refined astrometric calibration is performed at a later stage.

Another important generic routine was developed to recognize different types of exposures (calibration frames such as dome, sky flats and bias, photometric standard stars or science frames), reject bad frames and associate frames into pseudo-OBs to be reduced according to predefined prescriptions depending on their nature and passband. The association is based on the frame type and on the spatial separation and time interval between consecutive frames. Next, the removal of instrumental signatures such as bias subtraction, flat-fielding and de-fringing are carried out using identical procedures as those applied for infrared images as presented by Vandame et al. (2001). Some of the main features of the software worth mentioning are that the stacking of images is carried out in pixel space (see below), thereby allowing the optimal rejection of cosmic rays and bad pixels using sigma–clipping. Satellite tracks, quite frequent in wide-field images, are efficiently masked on the individual exposures using the Hough transform (Vandame 2001), thereby minimizing their impact on the final stacked image. The number of satellite tracks removed in a single passband ranges from 9 (e.g., R-band images) to 75 (U-band images) depending on the exposure time. In principle, other linear features such as diffraction spikes may also be treated in the same way. The net result of these new developments has been the production of remarkably clean final images, significantly superior to those of earlier releases. These results lead to the production of considerably more reliable source detections since the successful masking of features at the level of individual exposures dramatically minimizes the number of false detections in the final image. Finally, using the sky-flats, a first evaluation of the relative gains of the different chips is conducted for each passband, which it is later applied to the science frames. These relative gains vary from passband to passband and are, in some cases, especially in the UV, as large as 10%.

The stacking of the images is done in two distinct steps. First, the five images belonging to the same OB are warped to the first image of the OB, which is used as reference for the pixel based relative astrometry. All the images in the OB are then averaged. The second step involves warping all the co-added images corresponding to

each OB to an absolute astrometric reference catalog (see next section). The resulting images are then co-added taking into account their respective weight-maps, noise and flux scales. For this particular data set the warping of the images has been performed using the *nearest-neighbor* approach. The advantage of this warping is that the noise of the final image is uncorrelated. However, the astrometric solution is less precise due to discreteness effects. A new version of the warping has been developed allowing for a suite of kernel functions.

In contrast to other instruments (e.g., FORS), the fringing observed in I-band with WFI has a peak-to-peak amplitude of $\sim$10% relative to the background and varies on scales of hours. The de-fringing is performed in exactly the same way as for the infrared images, except that the number of frames in an OB is considerably smaller, making a good estimate harder. Currently, the residual contribution after de-fringing is comparable to the image noise. However, as in the case of the infrared, it would be preferable to decrease the integration time of each exposure and increase the number of dithered images. Based on the current findings, future I-band observations will be done using a different observing strategy.

The implementations described above make the EIS pipeline a tool capable of handling data from different telescope/instrument setups with different implementations of the FITS header. Finally, it is worth pointing out that using the available software several new developments are planned for the future. These include seeing deconvolution, morphological classification and difference image photometry for variability studies.

3.2. Astrometric calibration

The astrometric calibration of the images was performed using as the reference catalog a pre-release version of the *Guide Star Catalog-II* (GSC-II). The GSC-II (McLean et al. 2001) is based on multi-passbands all-sky photographic plate surveys including the Palomar Observatory Sky Survey (POSS-I-II), the SERC and the ESO Red Survey. The astrometric calibration of GSC-II has been obtained relative to Hipparcos (Perryman et al. 1997) and Tycho catalogs (Høg et al. 1997) and the *ACT* (Urban et al. 1998). The astrometric calibration was done using the method developed by Djamdji et al. (1993) based on a multi-resolution decomposition of images using wavelet transforms (MVM). An implementation of these algorithms to stack images, referred to as MVM-astrometry, has been done for EIS as is described above. This package has proven to be efficient and robust for pipeline reductions.

3.3. Photometric calibration

Magnitudes were calibrated to the Johnson-Cousins system using Landolt standards taken from Landolt (1992). While standard stars were observed on every night, to optimize the observing time most observations were used to monitor the zero-point of the night and to compute color terms. For the final calibration, three nights in October 2000, all photometric, were used to obtain measurements of standards over a broad range of airmasses. During these nights, a set of dithered images in each passband was taken overlapping two adjacent pointings (Deep2-b and Deep-2c). These were then used to set the absolute flux scale for all passbands, except the I-band due to problems with de-fringing. For this case, the night of Nov. 4 1999 was used to determine the I-band calibration.

Photometric solutions were obtained using the new EIS photometric pipeline which is fully integrated to the associated database. The tool provides a convenient environment to obtain, verify and store the results of the fits. In the interactive mode it is possible to fit the data after rejecting individual measurements, stars and chips. Alternatively, one can also easily obtain independent solutions for each chip. Unfortunately, the number of standards for the fields considered does not allow independent solutions for each of the eight chips. Therefore, the present calibration had to rely on solutions including all the available chips.

Magnitudes for Landolt stars were obtained using an aperture 6 arcsec in diameter, which proved to be adequate by monitoring the growth curve of all the measured stars. The accuracy of the zero-points are estimated to be in the range ± 0.03 mag to ± 0.08 mag, with the U-bands having the largest uncertainties. At face value, these results indicate that the gain correction applied to the different chips based on the flatfield exposures is adequate for most passbands with the possible exception of the U-band. A final determination of the relative gains will require a more careful monitoring of the amplitude of these corrections and chip-based solutions. A set of secondary stars for all the Landolt fields considered would also be extremely useful to always allow a chip-based calibration. Efforts in this direction are already underway by several groups.

The computed extinction coefficients compare well with those estimated from the mean extinction curve of the Chilean sites. Finally, the following color terms, relative to the Johnson-Cousins (JC) system, have been empirically determined:

$$
\begin{aligned}
(U_{\rm JC} - U'_{\rm EIS}) &= 0.04 \times (U-B)_{\rm JC},\\
(U_{\rm JC} - U_{\rm EIS}) &= 0.03 \times (U-B)_{\rm JC},\\
(B_{\rm JC} - B_{\rm EIS}) &= 0.14 \times (U-B)_{\rm JC},\\
(B_{\rm JC} - B_{\rm EIS}) &= 0.24 \times (B-V)_{\rm JC},\\
(V_{\rm JC} - V_{\rm EIS}) &= -0.11 \times (B-V)_{\rm JC},\\
(V_{\rm JC} - V_{\rm EIS}) &= -0.21 \times (V-R)_{\rm JC},\\
(R_{\rm JC} - R_{\rm EIS}) &= -0.04 \times (V-R)_{\rm JC},\\
(R_{\rm JC} - R_{\rm EIS}) &= -0.04 \times (R-I)_{\rm JC},\\
(I_{\rm JC} - I_{\rm EIS}) &= 0.25 \times (R-I)_{\rm JC}.
\end{aligned}
$$

These equations can be inverted to a more useful form, expressing the color terms as a function of the observed colors yielding:

$$
\begin{aligned}
(U_{\rm JC} - U'_{\rm EIS}) &= 0.04 \times (U' - B)_{\rm EIS},\\
(U_{\rm JC} - U_{\rm EIS}) &= 0.03 \times (U - B)_{\rm EIS},\\
(B_{\rm JC} - B_{\rm EIS}) &= 0.36 \times (B - V)_{\rm EIS},\\
(V_{\rm JC} - V_{\rm EIS}) &= -0.08 \times (B - V)_{\rm EIS},\\
(R_{\rm JC} - R_{\rm EIS}) &= -0.05 \times (V - R)_{\rm EIS},\\
(I_{\rm JC} - I_{\rm EIS}) &= 0.35 \times (R - I)_{\rm EIS}.
\end{aligned}
$$

These values have a typical error of ± 0.03 and are in good agreement with those computed using the response function of the filters considered, except for U' for which the difference in the color term can be $\sim$0.2 mag. This is because the UV-response of the system is at the time of writing still poorly determined.

The magnitudes were also corrected for galactic absorption, using $E(B-V) = 0.0089$ as derived from Schlegel et al. (1998), yielding $A_U = 0.05$ mag, $A_B = 0.04$ mag, $A_V = 0.03$ mag, $A_R = 0.02$ mag and $A_I = 0.02$ mag. All magnitudes have been converted to the AB system, unless otherwise specified, using the following relations: $U'_{AB} = U' + 1.04$; $U_{AB} = U + 0.80$; $B_{AB} = B - 0.11$; $V_{AB} = V$; $R_{AB} = R + 0.19$; and $I_{AB} = I + 0.50$.

3.4. Image products

The images being released are fully astrometrically (conical equal-area projection; COE) and photometrically calibrated (normalized to 1 s exposure time). The FITS files being provided include both the pixel and weight maps as FITS extensions. A stand-alone software tool to convert the COE images to best-fit TAN projection by modifying the image headers is available through the EIS web pages. The astrometric information is stored in the world coordinate system (WCS) keywords in the FITS headers. Similarly, the photometric calibration is provided by the zero-point and its error available in the header keywords ZP and ZP_ERR. The zero-point includes the normalized zero-point of the photometric solution and the atmospheric extinction correction. In the header one can also find a product identification number (P_ID) which should always be used as reference. The headers also provide information on the number of stacked frames and the on-source total integration time. Additionally, the seeing obtained by measuring the *FWHM* of bright stars in the final stacked images is stored in the header keyword SEE_IMA.

High-resolution images in the different passbands can be found at the URL "`http://www.eso.org/science/eis/`". The image quality of the final images can be assessed by investigating the nature and the amplitude of the PSF distortions. These are measured by using the two components of the so-called polarization vector. These components are derived from the major- (A) and minor-axis (B) and the position angle (θ) as measured by SExtractor for point-like sources using the following expressions:

$$
\begin{aligned}
e_1 &= \frac{A-B}{A+B}\cos(2\theta)\\
e_2 &= \frac{A-B}{A+B}\sin(2\theta).
\end{aligned}
$$

The quantities e_1 and e_2 give the amplitude of the distortion. As an illustration, Figs. 5 and 6 show the results obtained from the final R-band image, which consists 30 co-added WFI exposures. Figure 5 shows the distribution of the amplitude of the components, e_1 and e_2, for the individual point sources observed over the entire field and in Fig. 6 the polarization vector field smoothed over a scale of 7 arcmin. The scale of the amplitude of the vectors is set by the length of the small thick line shown on the upper left corner of the figure, which corresponds to an amplitude of 0.0015 (0.15%). These results attest to the excellent quality of the images produced by WFI, leading to a uniform and small PSF distortion throughout the frame with an rms amplitude $\lesssim$2%. Similar results are obtained for the other passbands.

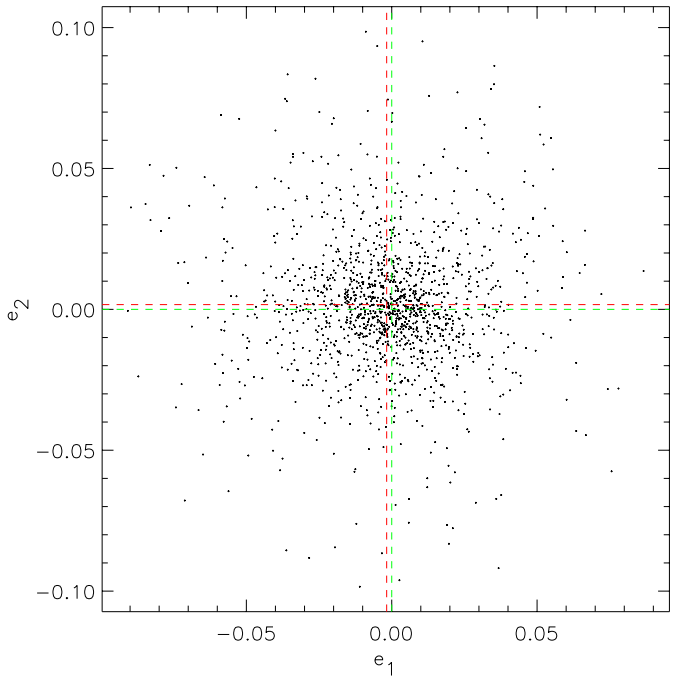

Fig. 5. Amplitude of the PSF distortion over the entire final R-band image. One line is centered on (0, 0), the other on the actual barycenter of the datapoints on (−0.002, 0.002).

4. Source lists

Source extraction was performed using the latest version of SExtractor software (Bertin & Arnouts 1996; ver. 2.2.1). This version resolves a subtle problem, first identified in the prompt release of the Pilot Survey, which caused the creation of regions devoid of sources when applying SExtractor to WFI frames with weights (Bertin 2001). Detection was carried out separately using the co-added

Table 7. First 40 entries of the CDF-S R-band source list (all magnitudes are given in the AB system).

#	α	δ	$m_{\rm tot}$	ϵ	$m_{\rm iso}$	ϵ	$m_{\rm aper}$	ϵ	S/N	A	$r_{\rm h}$	b/a	PA	class	Flag	EIS flag
EISJ033059.53-275901.2	03:30:59.53	-27:59:01.2	23.99	0.32	24.87	0.29	23.96	0.37	3.41	0.40	2.28	0.71	-12.27	0.78	24	2
EISJ033059.54-275849.0	03:30:59.54	-27:58:49.0	24.27	0.35	24.73	0.26	23.69	0.30	3.87	0.51	1.62	0.62	-52.69	0.69	24	2
EISJ033059.56-275842.9	03:30:59.56	-27:58:42.9	22.29	0.10	22.49	0.08	22.35	0.09	12.59	2.83	2.50	0.66	-6.50	0.85	24	2
EISJ033059.58-275555.1	03:30:59.58	-27:55:55.1	17.66	0.00	17.63	0.00	17.70	0.00	333.33	17.39	2.01	0.67	5.63	0.98	26	2
EISJ033059.62-275314.7	03:30:59.62	-27:53:14.7	22.44	0.09	22.57	0.08	22.39	0.09	13.28	1.76	1.91	0.74	-1.47	0.98	24	2
EISJ033059.65-275044.8	03:30:59.65	-27:50:44.8	22.96	0.18	23.36	0.13	23.00	0.16	7.63	1.53	2.35	0.54	-4.31	0.97	24	2
EISJ033059.66-275250.3	03:30:59.66	-27:52:50.3	22.40	0.18	23.33	0.15	22.86	0.16	6.58	1.87	4.50	0.54	9.65	0.93	16	2
EISJ033059.69-274812.7	03:30:59.69	-27:48:12.7	23.16	0.24	23.77	0.18	23.48	0.26	5.56	1.25	2.61	0.64	-18.88	0.96	24	2
EISJ033059.72-274830.3	03:30:59.72	-27:48:30.3	23.65	0.34	24.29	0.22	23.88	0.41	4.46	0.85	2.63	0.44	-34.08	0.95	16	2
EISJ033059.72-275620.2	03:30:59.72	-27:56:20.2	22.07	0.06	22.08	0.04	22.08	0.08	22.37	1.08	0.63	0.96	-7.29	1.00	16	2
EISJ033059.73-274928.3	03:30:59.73	-27:49:28.3	23.45	0.21	23.67	0.16	23.32	0.26	6.27	1.25	2.01	0.81	55.28	0.96	16	2
EISJ033059.74-275443.7	03:30:59.74	-27:54:43.7	23.27	0.31	23.99	0.20	23.41	0.28	5.07	1.02	2.95	0.63	-22.99	0.95	16	2
EISJ033059.77-274046.7	03:30:59.77	-27:40:46.7	23.62	0.28	24.68	0.27	23.90	0.34	3.72	0.62	3.15	0.32	-3.07	0.87	24	2
EISJ033059.78-274230.4	03:30:59.78	-27:42:30.4	24.15	0.37	25.01	0.31	23.80	0.35	3.22	0.45	1.84	0.79	45.09	0.78	16	2
EISJ033059.78-275538.8	03:30:59.78	-27:55:38.8	21.67	0.06	21.73	0.05	21.70	0.06	20.88	3.74	2.14	0.80	-63.37	0.98	16	2
EISJ033059.79-275147.7	03:30:59.79	-27:51:47.7	23.76	0.35	24.82	0.27	23.65	0.35	3.77	0.40	2.76	0.81	0.56	0.80	16	2
EISJ033059.80-274545.0	03:30:59.80	-27:45:45.0	23.00	0.25	24.02	0.21	23.15	0.22	4.85	0.85	3.54	0.64	-42.96	0.95	16	2
EISJ033059.81-274007.1	03:30:59.81	-27:40:07.1	22.99	0.15	23.15	0.12	22.96	0.16	8.10	1.98	2.24	0.85	-20.05	0.96	24	1
EISJ033059.82-275841.9	03:30:59.82	-27:58:41.9	23.70	0.32	24.18	0.21	23.56	0.32	4.79	0.85	1.98	0.73	-44.84	0.95	0	1
EISJ033059.83-273819.2	03:30:59.83	-27:38:19.2	20.50	0.03	21.14	0.03	21.38	0.03	31.55	5.32	7.04	0.24	3.98	0.12	19	1
EISJ033059.84-273644.5	03:30:59.84	-27:36:44.5	24.29	0.32	24.60	0.23	24.33	0.53	4.33	0.51	1.56	0.61	-36.14	0.88	24	1
EISJ033059.86-273500.1	03:30:59.86	-27:35:00.1	23.35	0.22	24.50	0.24	23.60	0.27	4.12	0.62	4.22	0.56	-3.94	0.94	24	1
EISJ033059.86-273816.7	03:30:59.86	-27:38:16.7	19.54	0.02	19.91	0.02	20.86	0.03	49.50	21.52	10.53	0.39	-21.38	0.03	19	1
EISJ033059.86-273912.9	03:30:59.86	-27:39:12.9	21.98	0.11	22.35	0.08	22.27	0.09	12.11	3.74	3.52	0.80	-59.73	0.27	19	1
EISJ033059.86-274540.4	03:30:59.86	-27:45:40.4	22.57	0.19	23.92	0.20	23.90	0.44	5.09	1.30	11.40	0.15	-0.45	0.99	17	1
EISJ033059.87-275530.7	03:30:59.87	-27:55:30.7	22.00	0.09	22.15	0.07	22.06	0.08	14.97	3.51	2.60	0.78	-51.62	0.76	0	1
EISJ033059.89-273831.6	03:30:59.89	-27:38:31.6	23.47	0.33	24.67	0.29	23.35	0.26	3.45	0.57	2.65	0.41	54.80	0.83	16	1
EISJ033059.89-273957.4	03:30:59.89	-27:39:57.4	23.67	0.26	24.65	0.27	23.50	0.30	3.67	0.62	2.56	0.36	82.30	0.87	16	1
EISJ033059.90-273314.3	03:30:59.90	-27:33:14.3	22.22	0.08	22.27	0.06	22.20	0.08	15.97	2.32	1.94	0.78	-2.79	0.98	24	1
EISJ033059.91-273809.8	03:30:59.91	-27:38:09.8	21.96	0.16	22.41	0.10	22.74	0.15	10.50	4.19	6.41	0.30	-24.84	0.17	19	1
EISJ033059.94-273706.4	03:30:59.94	-27:37:06.4	24.31	0.28	24.64	0.24	24.32	0.65	4.22	0.40	1.17	0.74	-22.64	0.86	16	1
EISJ033059.94-273443.2	03:30:59.94	-27:34:43.2	20.05	0.02	20.06	0.02	20.22	0.02	57.14	10.99	3.70	0.78	35.52	0.13	24	1
EISJ033059.94-274639.7	03:30:59.94	-27:46:39.7	21.83	0.13	22.37	0.08	22.25	0.10	12.09	3.68	4.34	0.72	-7.10	0.34	16	1
EISJ033059.94-275426.9	03:30:59.94	-27:54:26.9	23.92	0.27	24.66	0.27	23.83	0.41	3.66	0.62	2.47	0.26	35.24	0.87	0	1
EISJ033059.95-274650.0	03:30:59.95	-27:46:50.0	23.44	0.25	23.54	0.13	23.22	0.24	7.59	0.79	0.54	0.97	-34.86	0.67	0	1
EISJ033059.97-273531.2	03:30:59.97	-27:35:31.2	22.67	0.23	23.58	0.15	23.14	0.22	6.61	1.30	3.55	0.76	-3.84	0.97	16	1
EISJ033059.97-273818.5	03:30:59.97	-27:38:18.5	19.85	0.02	20.27	0.02	20.77	0.03	41.15	15.41	7.06	0.78	-43.06	0.03	19	1
EISJ033059.98-272943.1	03:30:59.98	-27:29:43.1	23.58	0.23	24.27	0.22	24.04	0.49	4.50	0.79	2.49	0.27	-84.78	1.00	24	1
EISJ033059.99-275040.3	03:30:59.99	-27:50:40.3	23.73	0.30	24.11	0.19	24.02	0.48	5.25	0.79	2.10	0.57	-72.21	0.95	0	1
EISJ033059.99-275906.7	03:30:59.99	-27:59:06.7	23.00	0.24	23.69	0.18	22.99	0.19	5.45	1.30	3.29	0.61	-60.89	0.97	0	1

image of each passband and field. The main parameters in the detection are the smoothing kernel, taken to be a Gaussian with a $FWHM$ equal to 0.8 of that of the PSF measured on the frame; the minimum number of connected pixels above the detection threshold, depending on the seeing taken to be between 8 and 12 pixels, and the SExtractor detection threshold, taken to be between 0.55 (for U) and 0.7 (R and I) depending on the seeing. As an illustration, the tabulation of the first 40 entries in the R-band source catalog is presented in Table 7. All magnitudes are given in the AB system. The table lists:

Column 1: the EIS identification name;

Columns 2 and 3: right ascension and declination (J2000.0);

Columns 4–9: total, isophotal and aperture (3 arcsec diameter) magnitudes and respective errors. The first two magnitudes correspond to the `mag_auto` and `mag_iso` magnitudes measured by SExtractor. The magnitudes have been corrected for Galactic extinction taken from Schlegel et al. (1998). The errors are those estimated by SExtractor and include only the shot-noise of the measured source and background counts. Only objects detected with signal to noise $S/N \geq 3$ (based on the isophotal magnitude errors) are included.

Column 10: an estimate of the S/N of the detection, from the inverse of the errors estimated for the isophotal magnitude;

Columns 11: the isophotal area A of the object in square arcsec;

Column 12: the half-light radius $r_{\rm h}$ in arcsec;

Columns 13 and 14: minor to major-axis ratio and the position angle;

Column 15: the stellarity index computed by SExtractor;

Column 16: SExtractor flags (see Bertin 1998);

Column 17: EIS flags; these flags are used to identify objects in regions with very low weight or close to bright objects. Objects detected in regions with weight $\geq$30% of the maximum weight (proportional to the total integration time) and not affected by bright stars have EIS flag = 0. Objects with weight <30%, located at the edges of the frame, have EIS flag = 1. Finally, EIS flag = 2 indicates that the object is located in a region masked out due to the presence of a bright object.

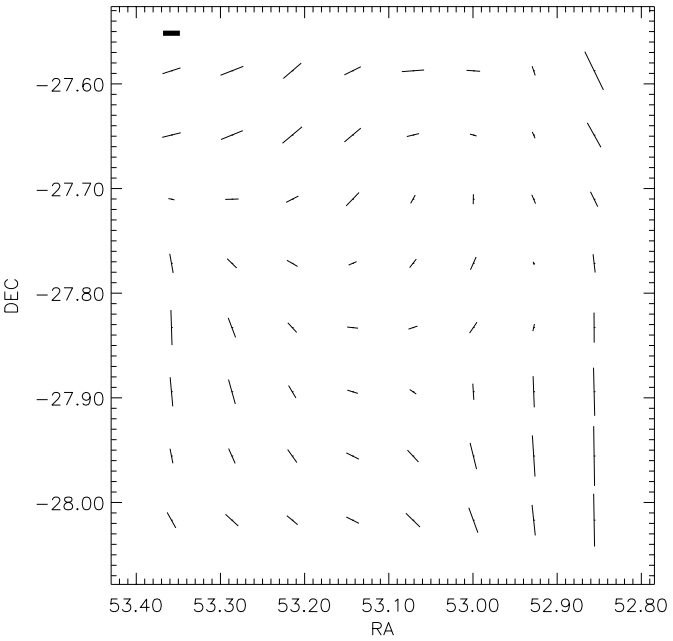

Fig. 6. Vector representation of the PSF distortions for the final R-band image smoothed over a scale of 7 arcmin. RA and DEC are in degrees. The amplitude of the vectors are scaled relative to the thick line segment shown on the upper left corner, which corresponds to an amplitude of 0.0015.

Similar tables for the other passbands are available upon request in ASCII format. Catalogs for the infrared mosaic and optical/infrared color catalogs will be distributed as soon as they become available. Note that besides distributing catalogs in tabular form as done here, catalogs in FITS formats will become part of the distribution of final products. From the inspection of the R-band weight map (see Fig. 3) one sees that, in contrast to catalogs extracted from single chip detectors, describing source catalogs drawn from multi-passband dithered observations of CCD mosaics requires significantly more information than can reasonably be provided in a single ASCII catalog. While the latter is adequate if the derived objects list is to be used for optical cross-identification, it is clearly not sufficient if one is interested in drawing statistical samples with well-defined limiting magnitudes and color coverage. To cope with these deficiencies, future releases will be made using FITS tables which will include: a FITS header with all the relevant information about the observations (pointing, filter, instrument), a FIELDS table which will include: the SExtractor parameters; the magnitude and stellarity index chosen for the star/galaxy classification; magnitude corrections (e.g., AB, extinction) appropriate for the filters used; a variety of limiting magnitudes (point source, turnover, completeness, spurious objects) including the brightest limiting magnitude to extract a homogeneous magnitude-limited sample; the effective area corresponding to this sample taking into account the area removed at the outer edges of the image based on the weight-map and the masks around bright objects, both now being produced automatically by the pipeline according to user-specified parameters. At the same time, no objects will be removed but will carry both their SExtractor and EIS flags, with the vertices of the corresponding masks also being included in the FITS catalogs in a specific fields table. This will also apply to color catalogs which, in addition to information similar to single passband catalogs, must also include others such as the definition of color context to clearly indicate the area of intersection of images in different passbands. In summary, the goal is to produce standard catalogs from which more complex analysis can be carried out with or without the images and associated weight maps.

The output of the new standardized procedures for single passband catalog production is shown in Fig. 7 for the catalog extracted from the final R-band image. The figure shows the outer bounding box defined based on the percentage of the peak exposure time one wants to consider and the masks around saturated or bright objects. Both the magnitude of the objects to be masked and the size of masks can be set by the user. In this example, one sees that not all possibly spurious sources can be eliminated automatically. In particular, in the lower right side of the figure (RA = 53.35, Dec = −27.9 degrees) one sees the effect of a ghost image of a bright star which produces a ring-shaped excess of objects. While attempts are currently being made to identify ghosts and automatically eliminate these regions, it is clear from the diversity of features that in practice, further by-hand clipping of the image is required depending on the specific application of the catalog. Tools for doing so are also implemented in the pipeline with the results being stored in the FITS catalog.

Each catalog produced by the pipeline goes through an automatic verification process which carries out several tests to check the reliability of the products by comparing them with other empirical data and model predictions. The results of some of these tests are described in the next section.

5. Discussion

5.1. Astrometry and photometry

In order to externally verify the accuracy of the astrometric calibration the source lists extracted from the different passbands were compared with that available from the 2MASS survey (Cutri et al. 2000). The number of objects found in common ranges from 286 to 415 depending on the passband considered. Using "good" objects, considering the various flags, in both catalogs the relative positions of coincident pairs were computed and the distribution of the differences in the case of the R-band is shown in Fig. 8. One finds an offset of about 0.12 arcsec in right ascension, a negligible shift in declination and an rms in the differences of $\lesssim$0.23 arcsec, independent of the passband considered. This shows that the astrometric solutions for the different passbands are essentially identical and an overall accuracy of $\sim$0.16 arcsec, probably limited to the internal

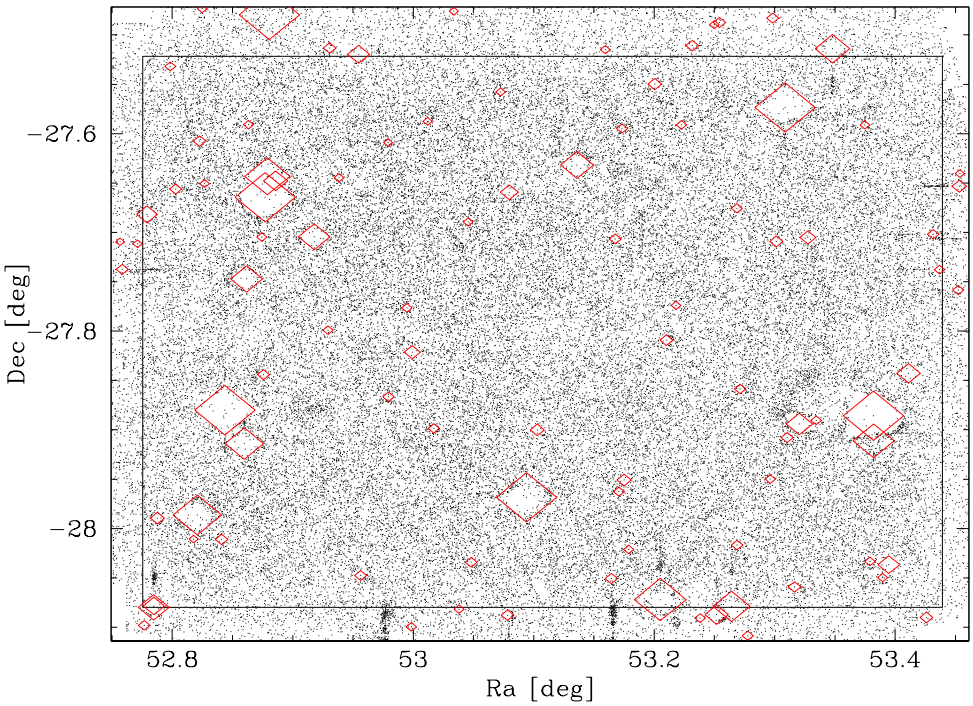

Fig. 7. Projected distribution of galaxies extracted from the R-band image. The figure shows the adopted frame and the masks automatically produced by the pipeline around bright objects which are used to set the EIS flags. It is important to emphasize that these parameters can be re-defined.

accuracy of the reference catalog, is achieved. Note that the shift of the optical data relative to 2MASS is smaller than that obtained with the infrared data. This, however, does not imply any inconsistency in the relative astrometry of the infrared and optical EIS data but rather it reflects the problem described in Vandame et al. (2001) with the astrometry of the pre-release of GSC-II. This problem will be fixed with the official release of the GSC-II.

An independent check of the astrometry can also be carried out by comparing the present astrometry with that determined by Wolf et al. (2001; COMBO survey) who recently obtained deep exposures of the same field in different passbands using the same instrument. In particular, their R-band data reaches $R = 26.0$ (Vega) at 5σ for a total integration time of 23 700 s. Within the overlapping area of both surveys, there are: ∼36 800 objects in common; ∼17 500 detected only by COMBO; ∼4400 only by EIS; and ∼4200 have multiple associations, which are not considered below. Figure 9 shows the result of the comparison of the positions for about 8500 objects in common. These objects include only objects with stellarity index >0.9 in the COMBO R-band source list and satisfying $R_{\rm EIS} < 25$ mag and $S/N({\rm EIS}) > 4$. From this comparison, one finds a relative offset of 0.15 arcsec in right ascension and −0.24 arcsec in declination, but more importantly a remarkably small rms of 0.12 arcsec in both directions, possibly suggesting an accuracy of $\lesssim$0.10 arcsec for each individual catalog. This is well within the requirements for slit/fiber positioning, a top requirement for the public survey. These results are insensitive to the exact way the sample is chosen.

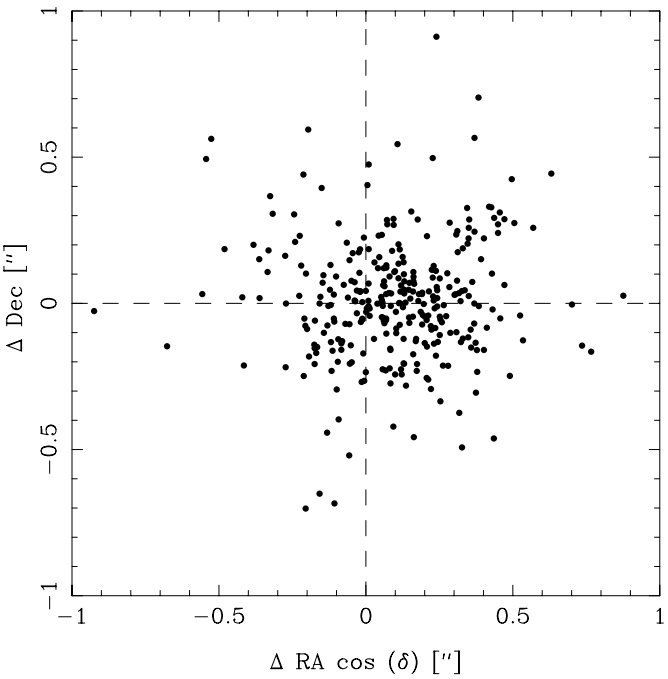

Fig. 8. Comparison in the R-band between the coordinates of objects in common with the 2MASS survey, offsets are computed as $EIS - 2MASS$.

The COMBO data also enables a comparison of the photometric calibration. Figure 10 shows the results of this comparison in the Vega system from which one finds a zero-point offset of ∼−0.01 with an rms of about 0.01 mag for $16 \lesssim R_{\rm EIS} \lesssim 20$ mag, while for objects brighter than

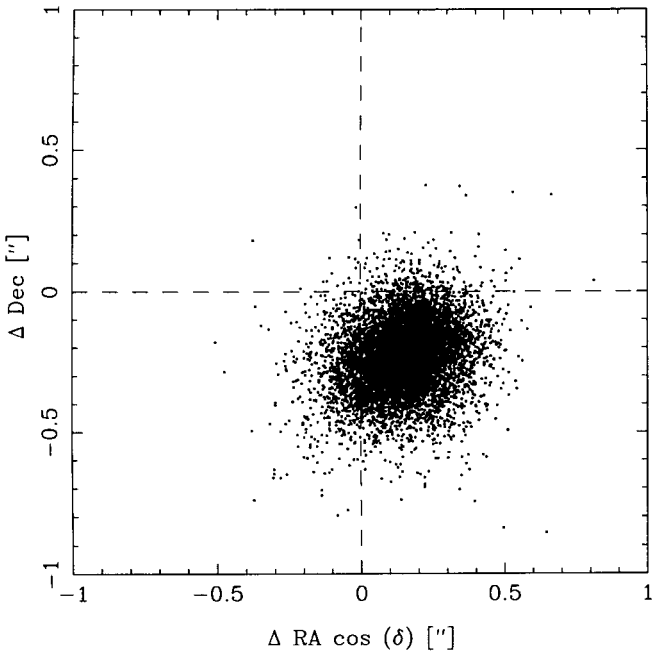

Fig. 9. Comparison between the location of objects in common with the COMBO survey, offsets are computed as EIS-COMBO.

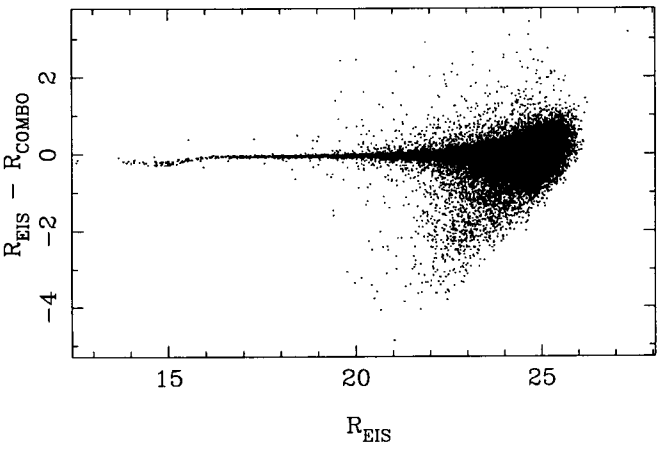

Fig. 10. Comparison between the measured R magnitudes of objects in common with the COMBO survey as a function of the $R_{\rm EIS}$ magnitude (Vega system).

$R \sim 16$ mag saturation sets in. For magnitudes fainter than $R \sim 20$ the scatter increases and beyond $R \sim 22$ one sees the Malmquist bias effect.

5.2. Number counts

A simple statistic that can be used to verify the overall characteristics of the derived catalogs and the parameters chosen for the star/galaxy classification is to compare the number counts of stars and galaxies with model predictions and other empirical data.

Figure 11 shows a comparison of the stellar counts as a function of the total magnitude (Vega system) with those obtained using the Galactic model described by Mendez & van Altena (1996), using the standard parameters described in their Table 1. Considering that no attempt has been made to choose model parameters to fit the observed counts, the agreement between observations and the model predictions is very good. In the B-band, where the present survey is deeper, there seems to be an excess of stellar objects. This is possibly due to QSOs, which are estimated to have a surface density of 120 objects per square degree per 0.5 mag interval at $B = 24$ (Hatziminaoglou et al. 2001). This effect is not expected in V and I because the surface density of QSOs at the magnitude where the stellar counts drop is expected to be small, of order 30–40 per square degree per 0.5 mag interval. Currently, the comparison of the star counts is only possible for the three passbands considered. However, this problem is being addressed and soon a more generic galactic model will be available in the EIS pipeline to compare the predicted counts in all passbands using the transmission curves for the filters being used in a given survey setup (Girardi 2001).

Similarly, Fig. 12 shows the comparison of galaxy counts as a function of the total magnitude, for each of the available passbands, with those obtained for other data sets. In this case, galaxies were defined as objects with a stellarity index less than 0.95 (0.90 in the I-band) or fainter than the classification limit of each passband. The sample includes only objects with $S/N > 3$ and with the appropriate SExtractor and EIS flags and the normalization of the counts takes into account the effective area of each catalog. The U-band counts of Guhathakurta et al. (1990) and I-band counts of Postman et al. (1998) have been corrected assuming an AB correction of 0.8 and 0.45, respectively. As can be seen the observed counts are in good agreement with previously published results indicating that the catalogs being distributed are statistically consistent.

5.3. Survey performance

The characteristics of the data obtained by the present survey are summarized in Table 8 which lists: in Col. 1 the filter; in Col. 2 the seeing of the final co-added image; in Cols. 3 and 4 the 5σ and 3σ limiting AB magnitude measured within an aperture $2 \times FWHM$; and in Col. 5 the number of objects with $S/N \geq 3$, i.e. the number of entries in the catalogs being distributed. At the 5σ limiting magnitudes the fraction of spurious objects with $S/N \geq 5$ is estimated to be $\lesssim$2% for all bands. The fraction of spurious objects was estimated by creating catalogs from the survey images multiplied by -1. The mock images were then used as input to the catalog production and from the comparison between the catalogs of the mock and real objects the fraction of false-positive detections was estimated.

The fact that the COMBO data reaches fainter magnitudes can also be used to obtain a first estimate of the completeness limit of the CDF-S data in the R-band. Figure 13

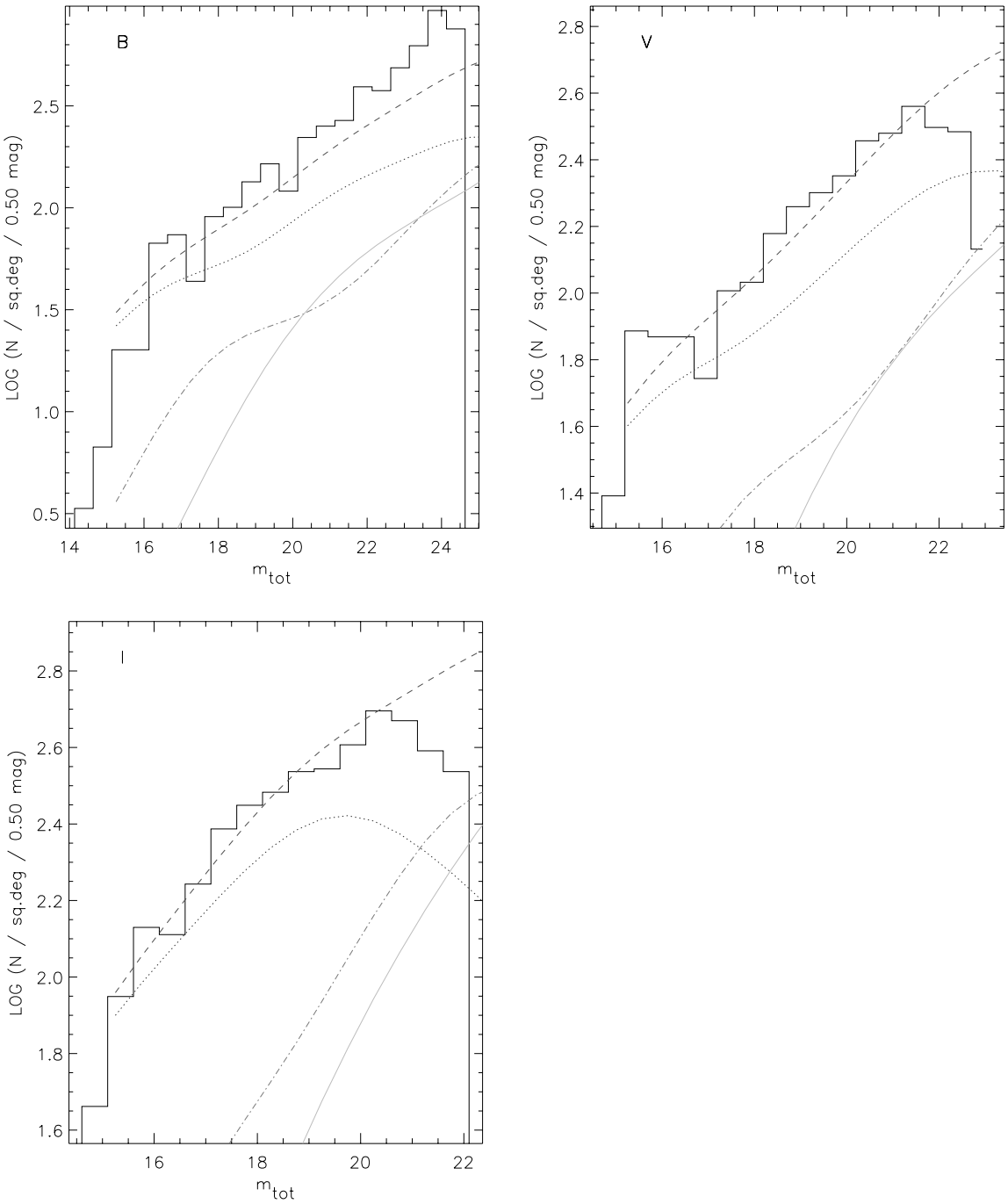

Fig. 11. Comparison of stellar number counts in B (top panel), V (middle panel) and I (lower panel) passbands obtained from the present work (histogram) and those based on the Galactic model of Mendez & van Altena (1996; long-dashed line). In this plot, the magnitudes are in the Vega system. The model includes an old disk population (short dashed line), a thick-disk component (dot-dashed line) and a halo component (dot-dot-dashed line).

shows the ratio as a function of the $R_{\rm COMBO}$ of objects in both catalogs. From this plot, one finds that the R-band catalog is complete to $R_{AB} \sim 24.7$ and 50% complete at $R_{AB} \sim 25.7$. This estimate is probably conservative. A first indication is that there are a large number of objects detected only in the data presented here, most of them at the faint end $R \gtrsim 25.2$. Second, the number of spurious detections at $R \sim 26$ is still relatively small ($\lesssim$30%). Clearly, a determination of the completeness of the catalog from the CDF-S data themselves is highly desirable and will be implemented in the near future.

The limiting magnitudes reached by the present observations are, in general, brighter than those originally proposed ($U_{AB} = 26.8; B_{AB} = 26.0; V_{AB} = 26.0; R_{AB} = 26.3; I_{AB} = 26.0$). For BVR, an increase of the integration time by a factor of two is required to reach the originally stated 5σ limits, representing a 50% increase in the total integration time requested per pointing. Certainly more

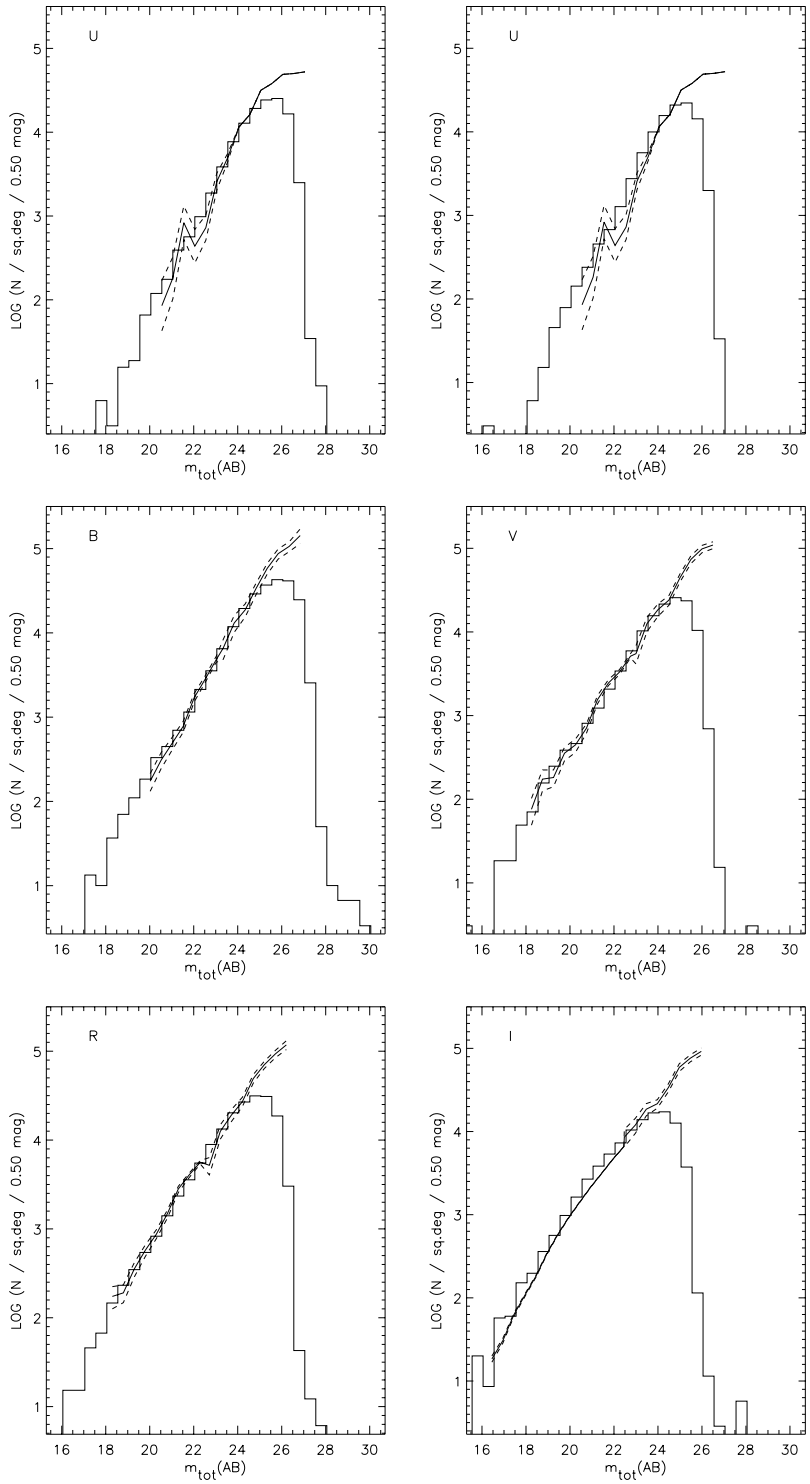

Fig. 12. Comparison of galaxy number counts from the present work (histograms) with those from the following authors: U-band: Guhathakurta et al. (1990); BVR-bands: Arnouts et al. (1997) and Arnouts et al. (1999); I-band: Postman et al. (1998) and Arnouts et al. (1999). The top left panel refers to U', while the top right panel to U. Solid lines represent the mean number counts and the dashed lines the associated errors.

serious is the requirements in U and I, even if more efficient filters are used. From the present data, one finds that the new U' filter has an efficiency at least 5% larger than the original U. A similar increase in efficiency in I is possible using a filter similar to the one available for EMMI for the EIS-WIDE survey. However, even with the new filters the time required to reach the desire magnitudes in U and I involve a large increase (a factor $\gtrsim$4) in their already long integration times. Such an increase would make the desired area coverage unattainable. On the other hand, the limiting magnitudes obtained by the present survey compare favorably with those reached by EIS-DEEP from

Table 8. Properties of the extracted CDF-S catalogs (*AB* system).

Filter	Seeing (arcsec)	$m_{\rm lim}(5\sigma)$ (mag)	$m_{\rm lim}(3\sigma)$ (mag)	$N_{\rm obj}$
U	0.98	25.7	26.3	37094
U'	1.06	26.0	26.6	42087
B	1.02	26.4	27.0	74827
V	0.97	25.4	26.0	45912
R	0.86	25.5	26.1	65148
I	0.93	24.7	25.3	43253

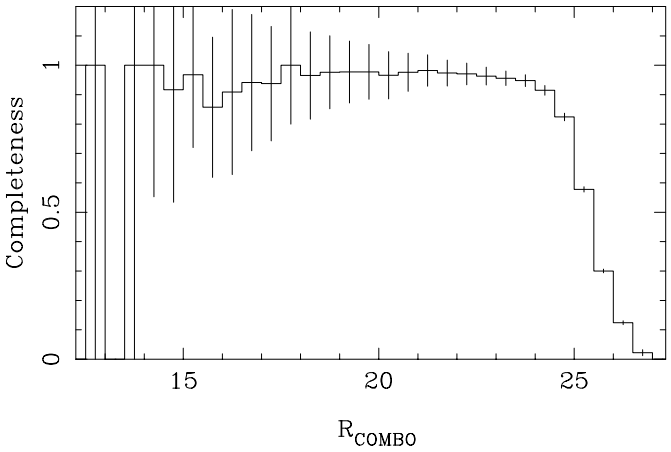

Fig. 13. Estimated completeness, and associated Poisson error, of the CDF-S R-band catalog as a function of the $R_{\rm COMBO}$ magnitude in the Vega system.

which Lyman-break galaxy candidates drawn from those samples (da Costa et al. 1998; Rengelink et al. 1998) have been successfully confirmed spectroscopically at $z \gtrsim 2.8$ (Cristiani et al. 2000), strongly suggesting that the primary goal of the present survey is indeed possible. A more detailed discussion of this point will be presented elsewhere when attempts to combine the data obtained using the two different U filters will be made (Arnouts et al. 2001; Benoist et al. 2001b).

Finally, as mentioned in Sect. 2, the CDF-S has already been observed both in optical and infrared passbands as part of the EIS-DEEP survey using the NTT (Rengelink et al. 1998). These old observations are being re-analyzed, using the new methods of the pipeline and compared with the present observations elsewhere (Benoist et al. 2001a). The infrared data from this survey is particularly important as it complements the infrared CDF-S survey recently completed (Vandame et al. 2001).

6. Summary

This paper presents the first optical results of the ongoing multicolor Deep Public Survey being conducted by the EIS program. The observations and the data for the first pointing completed as part of this program which corresponds to the Chandra CDF-S field are described. The set of products being publicly released includes fully calibrated pixel maps and source lists covering the CDF-S region. Given the current interest in this area of the sky both the optical data presented here, covering $\sim$0.25 square degrees, and the infrared survey recently released, covering an area of $\sim$0.11 square degrees, are being made available world-wide. Hopefully, this will, together with the Chandra X-ray data, contribute to making this region of the sky a natural target for multi-wavelength observations in the southern hemisphere and an ideal area for cosmological studies. Other derived products from the EIS program will be described in forthcoming papers in this series.

Acknowledgements. We thank all of those directly or indirectly involved in the EIS effort. Our special thanks to K. Meisenheimer and C. Wolf for making their U-band images and R-band catalogs available to EIS, E. Bertin for his quick response to our request for help, A. Bijaoui for allowing us to use tools developed by him and collaborators over the years and past EIS team members for building the foundations of this program. We would also like to thank A. Renzini and past and present members of the Working Group for Public Surveys. The Guide Star Catalogue-II is produced by the Space Telescope Science Institute in collaboration with the Osservatorio Astronomico di Torino. Space Telescope Science Institute is operated by the Association of Universities for Research in Astronomy, for the National Aeronautics and Space Administration under contract NAS5-26555. Additional support is provided by the Association of Universities for Research in Astronomy, the Italian Council for Research in Astronomy, European Southern Observatory, Space Telescope European Coordinating Facility, the International GEMINI project and the European Space Agency Astrophysics Division. This publication makes use of data products from the Two Micron All Sky Survey, which is a joint project of the University of Massachusetts and the Infrared Processing and Analysis Center/California Institute of Technology, funded by the National Aeronautics and Space Administration and the National Science Foundation. This research has made use of the SIMBAD database, operated at CDS, Strasbourg, France.

References

Arnouts, S., de Lapparent, V., Mathez, G., et al. 1997, A&AS, 124, 163
Arnouts, S., d'Odorico, S., Cristiani, S., et al. 1999, A&A, 341, 641
Arnouts, S., et al. 2001, in preparation
Benoist, C., et al. 2001a, in preparation
Benoist, C., et al. 2001b, in preparation
Bertin, E., & Arnouts, S. 1996, A&AS, 117, 393
Bertin, E. 1998, SExtractor, User's guide, v2.0
Bertin, E. 2001, private communication
Cristiani, S., Appenzeller, I., Arnouts, S., et al. 2000, A&A, 359, 489
Cutri, R. M., Skrutskie, M. F., Van Dyk, S., et al. 2000, Explanatory Supplement to the 2MASS Second Incremental Data Release
da Costa, L., et al. 1998, A&A, submitted [astro-ph/9812105]

da Costa, L. N., et al. 1999, The Messenger, 98, 36
da Costa, L. N. 2001, in Mining the Sky, Proc. of ESO Workshop (Springer-Verlag), 521
Djamdji, J. P., Bijaoui, A., & Manière, R. 1993, Photogrammetric Engineering and Remote Sensing, 59, 645
Giacconi, R, Rosati, P., Tozzi, P., et al. 2001, ApJ, 551, 624
Girardi, L. 2001, private communication
Guhathakurta, P., Tyson, J. A., & Majewski, S. R. 1990, in Evolution of the universe of galaxies, Astronomical Society of the Pacific, 304
Hatziminaoglou, E., et al. 2001, A&A, submitted
Høg E., Bässgen, G., Bastian, U., et al. 1997, A&A, 323, L57
Landolt, A. U. 1992, AJ, 104, 340
McLean, B., Greene, G., Lattanzi, M., & Pirenne B. 2001, Astronomical Data Analysis Software and Systems IX, ed. N. Manset, C. Veillet, & D. Crabtree, ASP Conf. Proc., 216, 145
Mendez, R. A., & van Altena, W. F. 1996, MNRAS, 279, 1357
Momany, Y., Vandame, B., Zaggia, S., et al. 2001, A&A, 379, 436
Perryman, M. A. C., Lindegren, L., Kovalevsky, J., et al. 1997, A&A, 323, L49
Postman, M., Lauer, T. R., Szapudi, I., & Oegerle, W. 1998, ApJ, 506, 33
Rengelink, R., et al. 1998, A&A, submitted [astro-ph/9812190]
Rosati, P. 2001, in preparation
Schlegel, D., Finkbeiner, D., & Davis, M. 1998, ApJ, 500,525
Urban, S. E., Corbin, T. E., & Wycoff, G. L. 1998, AJ, 115, 2161
Vandame, B., Olsen, L. F., Jørgensen, H. E., et al. 2001, A&A, submitted [astro-ph/0102300]
Vandame, B. 2001, in Mining the Sky, Proc. of ESO Workshop (Springer-Verlag), 595
Wolf, C., Meisenheimer, K., Dye, S., et al. 2001, A&A, 377, 422